Formation of tabular single-domain magnetite induced by *Geobacter metallireducens* GS-15

Hojatollah Vali*†‡§, Benjamin Weiss¶‖, Yi-Liang Li, S. Kelly Sears*‡, Soon Sam Kim††, Joseph L. Kirschvink¶, and Chuanlun L. Zhang****

*Department of Anatomy and Cell Biology and ‡Facility for Electron Microscopy Research, McGill University, Montréal, QC, Canada H3A 2B2; †Department of Earth and Planetary Sciences, McGill University, Montréal, QC, Canada H3A 2A7; ¶Division of Geological and Planetary Sciences and ††Jet Propulsion Laboratory, California Institute of Technology, Pasadena, CA 91125; ‖Department of Earth, Atmospheric, and Planetary Sciences, Massachusetts Institute of Technology, Cambridge, MA 02139; and **Savannah River Ecology Laboratory, University of Georgia, Aiken, SC 29803

Edited by Russell J. Hemley, Carnegie Institution of Washington, Washington, DC, and approved October 4, 2004 (received for review June 7, 2004)

Distinct morphological characteristics of magnetite formed intracellularly by magnetic bacteria (magnetosome) are invoked as compelling evidence for biological activity on Earth and possibly on Mars. Crystals of magnetite produced extracellularly by a variety of bacteria including *Geobacter metallireducens* GS-15, thermophilic bacteria, and psychrotolerant bacteria are, however, traditionally not thought to have nearly as distinct morphologies. The size and shape of extracellular magnetite depend on the culture conditions and type of bacteria. Under typical CO_2-rich culture conditions, GS-15 is known to produce superparamagnetic magnetite (crystal diameters of approximately <30 nm). In the current study, we were able to produce a unique form of tabular, single-domain magnetite under nontraditional (low-CO_2) culture conditions. This magnetite has a distinct crystal habit and magnetic properties. This magnetite could be used as a biosignature to recognize ancient biological activities in terrestrial and extraterrestrial environments and also may be a major carrier of the magnetization in natural sediments.

Minerals must crystallize within one of the seven known crystallographic systems. Within each crystal system, a mineral may assume several crystalline forms. Changes in growth conditions such as impurities, pH, redox potential (Eh), ionic strength, temperature, and pressure may influence the habit of the crystal. Crystals belonging to the cubic crystal system such as magnetite (Fe_3O_4) are not expected to show any shape anisotropy when grown as free particles in aqueous solutions at room temperature. However, the possibility of deviation from the ideal morphological symmetry of the cubic system under specific environmental conditions (e.g., an anisotropic medium) has been reported (1, 2). Although magnetite forms predominantly diamond-shape octahedrons {111} in the cubic crystal classes, it also crystallizes in several other forms (e.g., dodecahedral and cubic). Unusual, elongated forms known as whiskers have also been reported to form from a vapor phase at high temperatures (3). Magnetite crystals formed by magnetotactic bacteria (magnetosomes) also have a variety of distinct morphologies. In particular, prismatic, elongated single-domain (SD) magnetite is produced intracellularly by a variety of magnetic bacteria in diverse environments (4–6). The formation of prismatic magnetite crystals has not been reported by any other mechanism at low temperature (<100°C). Extracellular biogenic magnetite is formed by several types of bacteria (7, 8), but is typically poorly crystalline and close to diamond and other equilibrium shapes such as cubes, octahedrons, and dodecahedrons.

Geobacter metallireducens GS-15 is known to produce fine-grained, predominantly superparamagnetic (10–50 nm in diameter) magnetite crystals under anaerobic conditions (9, 10). This magnetite is formed extracellularly during cell growth, but with no visible association with cellular structures. GS-15 is capable of rapid iron reduction at the expense of acetate as a carbon source (11). Depending on the cell culture conditions (e.g., composition of growth medium), siderite may also precipitate. The ratio of magnetite-to-siderite is controlled by the concentration of CO_2 in the head space of the culture tube and a carbonate buffer in the medium. Under conventional cell culture conditions, there is no intermediate phase between the final run-products, magnetite and siderite, and the starting material, ferrihydrite. Our objective in this study was to investigate the run-products in a GS-15 culture incubated in a low-CO_2 environment.

Materials and Methods

G. metallireducens GS-15 was obtained from the laboratory culture collection of John D. Coates, University of California, Berkeley. It was originally isolated from iron-rich sediments collected from the Potomac River (12) and was categorized in the delta proteobacteria, which are closely related to *Desulfuromonas acetoxidans* (13).

Ferrihydrite, which was prepared following a procedure described by Schwertmann and Cornell (14), was used as the sole electron acceptor for GS-15. Standard anaerobic techniques were used throughout the experiments. All transfers were performed by using needles and syringes under sterile conditions. The basal medium used for the incubation of GS-15 was composed of 0.25 g of NH_4Cl, 0.1 g of KCl, 5 g of Pipes (buffer), 5 ml of vitamin stock solution, and 5 ml of mineral stock solution added to 1 liter of second-order deionized water. After bubbling with N_2 gas, the medium was cooled with ice water to avoid negative pressure in the tubes. The medium was dispensed in 10-ml amounts in 26-ml pressure tubes with the protection of N_2 flow. The tubes were capped with butyl rubber stoppers, sealed with aluminum caps, and autoclaved at 121°C for 20 min. The pH of the media was adjusted to 7.2 before autoclaving. No phosphate was added to the media.

Preparation of Fe-Free Inoculum and Inoculation. Sodium acetate and ferric citrate (previously prepared stock solution) were used as the electron donor and electron acceptor (10 and 50 mM, respectively) for preparing the inoculum of GS-15. After incubating for 5 days, the GS-15 primary culture was pelletized by centrifuging the medium at 10,000 × *g*. After decanting the supernatant, the pellet was washed with O_2-free water to remove excess Fe(II) and redispersed in medium under anaerobic conditions. Nitrilotriacetic acid (NTA) (4 mM), 12.5 mM sodium acetate, 2.5 mM $FeCl_2$, 50 mM ferrihydrite, and 10% (vol/vol) inoculum were injected into the pressure tubes. All tubes were incubated at 30°C. $FeCl_2$ was added before incubation to accelerate the precipitation of magnetite. NTA was used to keep the Fe(III) added as free ions (15).

One milliliter of the cultured medium was taken from each tube at every sampling point for bacterial cell counts. The

This paper was submitted directly (Track II) to the PNAS office.

Abbreviations: TEM, transmission electron microscopy; SD, single domain; FMR, ferromagnetic resonance; Eh, redox potential; FC, field cool; ZFC, zero FC.

§To whom correspondence should be addressed. E-mail: vali@eps.mcgill.ca.

subculture was fixed with 2.5% glutaraldehyde in 0.1 M cacodylate. Cell numbers were determined by acridine-orange direct counts following the procedure described by Zhang *et al.* (16).

Time-Course Measurements of Iron Reduction. A 0.2-ml sample was taken from a set of tubes, transferred to oxygen-free 0.5 M HCl, and allowed to dissolve for 1 h. The solution was passed through a 0.2-μm filter and diluted with a ferrozine solution (1 g ferrozine and 13.7 g Hepes sodium salt in 1 liter of deionized water). Absorptions were measured on a Shimadzu UV-VIS spectrophotometer at 562 nm.

Magnetic Methods. The magnetic properties of the bacterial samples were measured at temperatures ranging from 10 to 300 K by using low-temperature superconducting quantum interference device, hysteresis loops, and ferromagnetic resonance (FMR) spectroscopy as described (17).

Transmission Electron Microscopy (TEM) Analysis. The morphological characteristics of magnetite were investigated with TEM. Culture medium containing bacterial cells, organic matter, and inorganic solids was fixed with 2.5% glutaraldehyde in 0.1 M cacodylate. The specimens were centrifuged for 2 min at 15,000 $\times$ *g* to form a pellet. After washing with buffer and a solution of 95% ethyl alcohol–H_2O, samples were dehydrated with 95% ethyl alcohol, and the pellet was embedded in low viscosity, thermally curing Epon resin. Ultrathin sections (70–80 nm) were cut from the resin blocks by using a Reichert-Jung Ultracut E ultramicrotome with a Diatome (Biel, Switzerland) diamond knife. The sections were transferred to 300-mesh formvar Cu TEM grids for image analysis in a JEOL JEM-2011 TEM equipped with a Gatan (Pleasanton, CA) 300W charge-coupled device camera. To enhance contrast in the bacterial cells in the TEM images, selected samples were stained with lead citrate and uranium acetate. Owing to the high concentration of organic matter in the biomass and interaction among magnetite crystals, a dispersion and suspension of the particles directly onto TEM grids was not possible.

The morphological descriptions of the crystals in the run-products as imaged in TEM are based on the 2D projections of the true crystal habits of individual particles. The 3D morphology of the crystals was assessed in TEM through a series of images at various angles of tilt (+45° to −45°). In addition, as the TEM images were obtained from ultrathin sections, it is expected that particles >70 nm would be fragments, which precludes a statistical analysis of the sizes and distribution of the particles.

Results and Discussion

Formation of Lepidocrocite (γ-FeOOH). Although the absence of CO_2 prevented the formation of siderite, an additional consequence was a distinct phase transformation and unique crystallization pathway. We found that when CO_2 was absent from GS-15's cell culture headspace, the ferrihydrite starting material transformed to lepidocrocite (γ-FeOOH) as an intermediate phase before evolving to magnetite (see below). The experiments ran for 34 days, and samples were taken at reaction times of 0, 24 h, 60 h, 125 h, 150 h, 558 h, 668 h, and 34 days. Control samples run under the same experimental conditions but without bacteria were sampled at the same reaction times. The Eh-pH show moderate change over the course of the experiments (Fig. 1). The results of TEM, x-ray powder diffraction (XRD), and magnetic analyses of two selected reaction times (150 and 668 h) and one control reaction time (668 h) are described herein in greater detail. The solid phase in the control sample consisted solely of ferrihydrite with no other mineral phase detected by TEM or XRD. The XRD data on the 150-h sample showed the predominance of lepidocrocite with minor amounts of magnetite

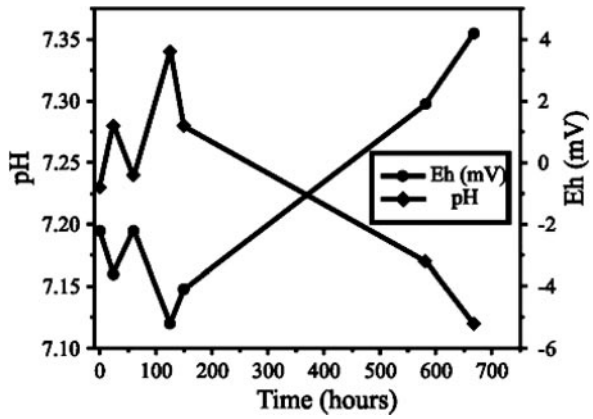

Fig. 1. Time-course analysis of pH and Eh showing minimal variation of both pH (7.10–7.35) and Eh (−4 to +4 mV) throughout the experiment. Note that the system becomes slightly oxidizing after 400 h, when magnetite becomes the predominant phase.

(Fig. 2*A*), whereas the 668-h sample showed only magnetite (Fig. 2*B*). Imaging of the 150-h sample by TEM showed the presence of relatively large, platy crystals of lepidocrocite surrounded by nanoparticle aggregates of ferrihydrite. Selected-area electron diffraction of the lepidocrocite showed single-crystal patterns (Fig. 3*A*). Minor amounts of superparamagnetic and SD magnetite were embedded within the aggregates of ferrihyderite. The crystals of lepidocrocite showed evidence of dissolution and were completely converted to magnetite by 668 h (Fig. 3*B*). Bacterial activity with respect to iron reduction was very low up to 125 h. An increase in Fe(II) in solution at 150 h indicated increased bacteria growth. The Fe(II) was consumed to form magnetite. As the magnetite continued to form until the end of the experiment, Fe(III) reduction by bacteria also continued. The presence of a biomass consisting of bacteria and their metabolic by-products was confirmed by TEM observation.

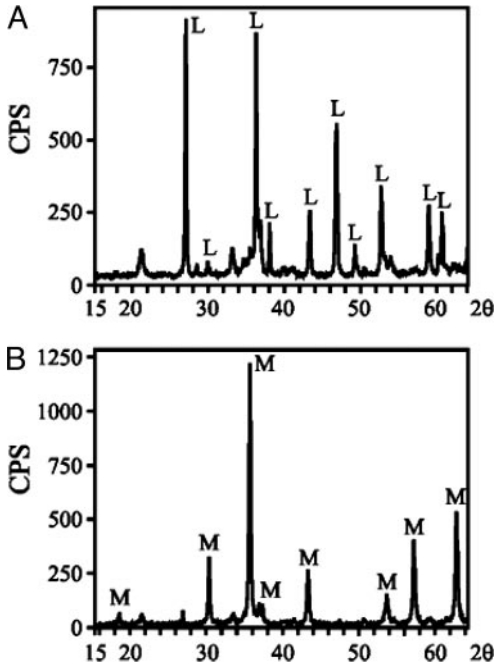

Fig. 2. X-ray diffraction patterns confirming the presence of lepidocrocite (L) in the sample at 150 h (*A*) and predominately magnetite (M) after 668 h (*B*). CPS, counts per second.

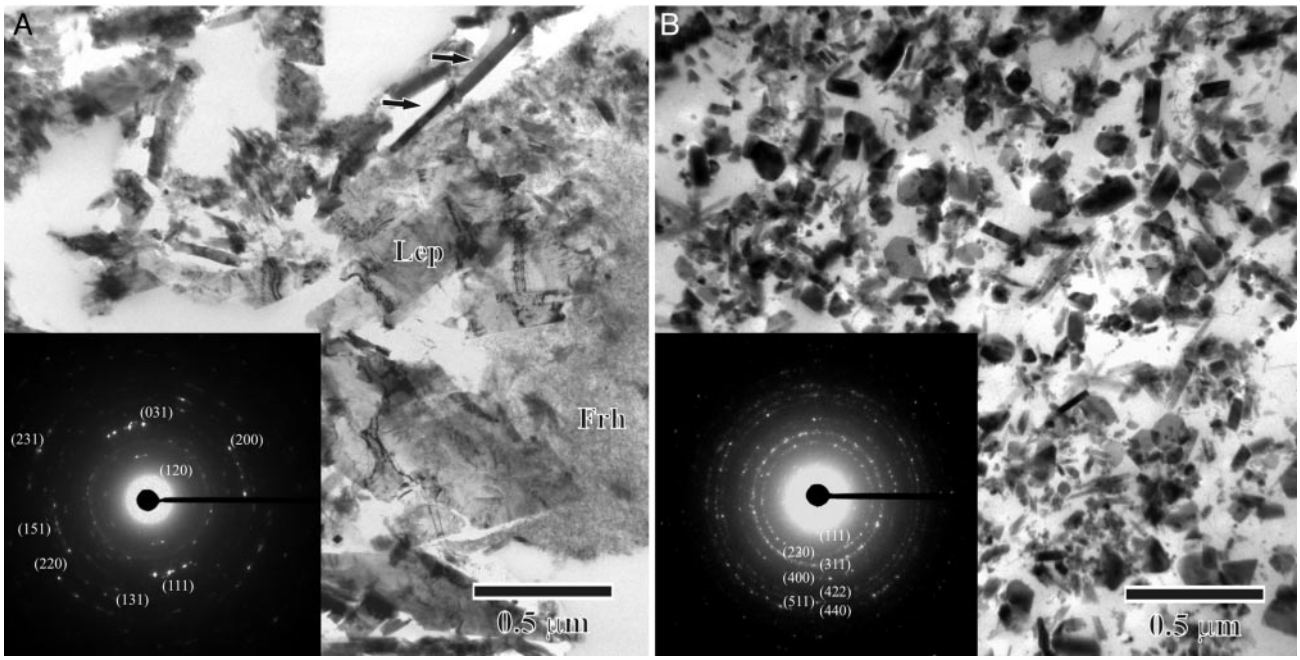

Fig. 3. Conventional TEM images obtained from ultrathin sections of the samples. (*A*) The samples at 150 h showed the presence of amorphous ferrihydrite (Frh) and crystalline plate-like lepidocrocite [Lep, the lath-shaped crystals (arrows) are cross sections of the plate-like lepidocrocite crystals]. (*Inset*) The selected-area electron diffraction pattern showing the presence of large single crystals of lepidocrocite (indices) and weak diffraction rings of fine-grained magnetite. (*B*) The samples at 668 h showed different projections of the tabular magnetite ranging from lath-like to platelet and diamond (equilibrium) shaped magnetite. (*Inset*) The selected-area electron diffraction pattern of an aggregate of magnetite with random orientation showing varying intensities of the diffraction rings and their corresponding indices.

The Moskowitz test (17–19) on the 150-h sample (Fig. 4*A*) showed a monotonic drop in remanence from room temperature to 10 K, a superimposed weak Verwey transition in the field cool (FC) curve at 118 ± 2 K, and $\delta_{FC}/\delta_{ZFC} = 1.1$, where ZFC is the zero FC. These data are consistent with most of the magnetism in this sample originating from a paramagnet [almost certainly the lepidocrocite, whose 50-K Néel point (20) would account for the observed steep drop in remanence to 50 K] along with a small fraction from magnetite in the SD or larger size range. That magnetite is quite pure: $Fe_{3-x}Z_xO_4$ with $x \approx 0.01$–0.04 for a wide range of impurities; Z = Zn, Ti, Al, Mg, Co, Ni, and Ga (20–23). The near-unity δ_{FC}/δ_{ZFC} value indicates the absence of isolated chains of crystals like those grown intracellularly by magnetotactic bacteria. X-band FMR spectra for the 150-h sample (Fig. 4*B*) had $g_{eff} = 2.1$ and $\Delta B =$ 77 mT. Although we are not aware of any previous FMR measurements on lepidocrocite, the sample's relatively narrow linewidth and g_{eff} value close to the 2.1 were distinct from typical SD magnetite samples (Fig. 4 *C* and *D*).

Lepidocrocite precipitates as a metastable phase under both natural and laboratory conditions (24). In soil, lepidocrocite forms by the oxidation of Fe^{2+} compounds. High partial pressures of CO_2 appear to preferentially favor goethite formation instead of lepidocrocite (14), as is also evident in our experiment. The Eh-pH (−4 mV − 7.28) data obtained from our experiment, however, does not fit into the stability field of lepidocrocite in the conventional Eh-pH (100–300 mV → 7) stability diagram (8, 26). This discrepancy may be explained by the biogenic origin of lepidocrocite that is mediated by the metabolic activity of GS-15. At the inorganic–organic interface, similar crystal growth of γ-FeOOH has been observed in the presence of a stearyl alcohol (Langmuir) monolayer, which serves as a template for the epitactic growth of γ-FeOOH (27). Banfield *et al.* (28) suggested that ferrihydrite converts to goethite via the relocation of iron atoms into adjacent face-sharing octahedral sites. A similar pathway may exist for the conversion of ferrihydrite to lepidocrocite.

Formation of SD Magnetite (Fe_3O_4). By 558 h, both the lepidocrocite and ferrihydrate were converted into magnetite. The x-ray powder diffraction data of the samples at 558 and 668 h revealed the presence of only magnetite (Fig. 2*B*). TEM investigation of these samples showed predominantly SD magnetite, as confirmed by the selected-area electron diffraction patterns (Fig. 3*B*). Images of the 2D projection of the crystals revealed the presence of a variety of shapes ranging from lath-like (aspect ratios from 1 to 0.25) to tabular platelet (pseudohexagonal) to diamond (equilibrium). Upon tilting of the specimen in TEM (±40°), some crystals showed an apparent change in shape, which is the result of the projection of the same tabular crystals having different orientation relative to the direction of the electron beam. Fig. 5 *A* and *B* shows the apparent changes in morphology of several tabular crystals at angles of tilt of 0° and 40°, respectively. High-resolution TEM images of one of the crystals viewed parallel to {111} shows a *d*-spacing of 0.48 nm, which is characteristic of magnetite (Fig. 5 *C* and *D*). Most of the tabular crystals show a unique twinning along the {111} plane (Fig. 5 *A* and *C*). There was an apparent wide size distribution in all shapes of magnetite from the three experiments. In general, among SD magnetite 70% of the particles consisted of tabular-shaped crystals that ranged in size from 20 to 200 nm in length and from 20 to 70 nm in width. These values are approximate as some crystals represent fragments of larger crystals from the process of ultrathin sectioning, which affects the measurement of the length of the crystal. Not all of the crystals are projected with the (111) parallel to the electron beam, which results in variation of the width. The aspect ratios of the tabular crystals were assessed by measuring the length of the larger crystals, which were projected with their (111) parallel to the beam. The fraction of diamond-shaped (equilibrium) magnetite crystals collected

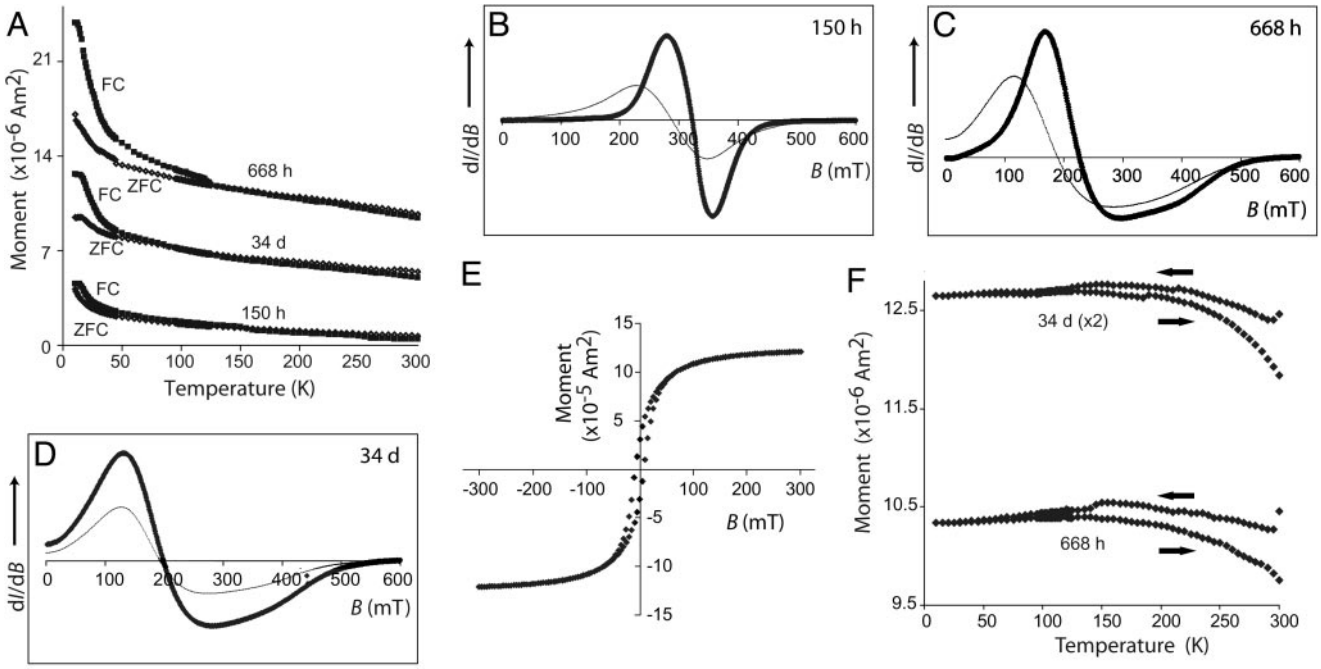

Fig. 4. Magnetic data on *G. metallireducens* GS-15 samples at various growth stages. (*A*) Moskowitz test on 668-h, 34-day, and 150-h samples. Shown is the moment as a function of temperature as the sample warmed up to room temperature (see text). (*B–D*) FMR spectra of: 150-h sample (*B*), 668-h sample (*C*), and 34-day sample (*D*). Shown is the derivative of the microwave (9.3 GHz) absorbance with respect to the intensity of the applied DC field, d*I*/d*B*, plotted as a function of the intensity of the field. Heavy lines indicate 295-K data; fine lines indicate 77-K data. (*E*) Low-temperature cycling of the 668-h and 34-day (data multiplied by 2) samples after exposure to a saturating (5 T) field at 300 K. Shown are the moments of the samples in a quenched ($<2 \times 10^{-4}$ T) field as they progressively cooled from 300 to 10 K (top curves) and then warmed back up to 300 K (bottom curves). The FC (■) and ZFC (◇) data are marked. (*F*) Room temperature hysteresis data on 34-day and 668-h samples.

after 34 days was slightly larger than that for the 558- and 668-h experiments. Energy dispersive spectroscopy of individual magnetite crystals did not reveal the presence of any detectable impurities.

The room temperature magnetic data favor the conclusion reached with our TEM data that the 668-h and 34-day samples contain predominantly SD to pseudo-SD magnetite. Hysteresis data at 295 K on the 668-h sample (Fig. 4*E*) indicated the presence of SD magnetite and showed a saturation field of 300 mT, a bulk coercivity of $H_c \approx 8$ mT, and a ratio of saturation remanence to saturation magnetization of $M_{rs}/M_s \approx 0.26$. Room temperature X-band FMR of the samples at 668 h measured $g_{eff} = 2.9$, $\Delta B = 129$ mT, and $A = 1.3$, consistent with the presence of interacting SD magnetite (Fig. 4*C*). These are very close to the values measured on the 34-day sample: $g_{eff} = 2.9$, $\Delta B = 108$ mT, and $A = 1.2$ (Fig. 4*D*).

Additional support for the presence of magnetite comes from our low-temperature magnetic data. Low-temperature cycling (Fig. 4*F*) and Moskowitz tests (Fig. 4*A*) suggest that the 668-h and 34-day samples undergo soft Verwey transitions. The moments of the two samples at 300 K (after warming) are ≈90% of that before cooling (Fig. 4*F*), which is consistent with an average grain size of approximately <100 nm (17, 19). The FC and ZFC curves (Fig. 4*A*) split at 122 ± 3 K (668-h sample) and ≈115 ± 10 K (34-day sample). The relatively large uncertainty on the latter results from the fact the ZFC curve actually crosses the FC curve (the meaning of this crossover is unclear). If we attribute this splitting to the Verwey transition, then the Moskowitz test suggests that the magnetite in these samples is quite pure: $Fe_{3-x}Z_xO_4$ with $x < 0.05$ for a wide range of impurities Z (see above). The sharp rise in remanence in the Moskowitz tests (Fig. 4*A*) just below 50 K likely reflects the presence of some lepidocrocite and/or a small fraction of superparamagnetic magnetite (24).

These magnetic data distinguish our GS-15 samples from those grown by conventional GS-15 culture methods (9). The latter typically have much lower remanence and coercivity ($M_{rs}/M_s \approx 0.02$ and $H_c = 0.8$ mT) (18) and have $g_{eff} = 2.07$, $\Delta B = 54$ mT, and $A = 1.03$ at room temperature (23), reflecting the fact they are almost entirely superparamagnetic in size. The 668-h and 34-day samples are also unlike magnetotactic bacteria, which typically have $\delta_{FC}/\delta_{ZFC} > 2$, $M_{rs}/M_s \approx 0.5$, $A < 1$, $\Delta B > 80$ mT, and secondary absorption peaks, which are thought to be a reflection of their intracellular chains of SD magnetite crystals (19, 23). Other than GS-15 grown under the conditions discussed here, only one other bacterium (the fermentative anaerobe *Thermoanaerobacter ethanolicus* TOR 39) is known to produce extracellular magnetite predominantly in the SD-size range (7, 23).

Biological-Induced Nucleation and Growth of Magnetite. Although there is extensive literature available on the synthesis of magnetite on inorganic and organic substrates, the role of bacteria in the formation of extracellular magnetite remains poorly understood. The primary driving force in biological-induced mineralization is the interaction between organic and inorganic phases. At the organic–inorganic interface, several factors may act in concert to control nucleation and growth of crystals, particularly pH, ionic strength, lattice geometry, polarity, stereochemistry, and topography (29, 30).

Newman and Banfield (31) discussed the molecular and biochemical processes involved in electron transfer and iron reduction in a bacteria-mediated aqueous system that are essential for extracellular precipitation of Fe(II)-containing phases such as magnetite. Lovley and coworkers (9, 10, 12, 13) have extensively investigated the roles of enzymatic and metabolic activities relevant to magnetite formation in GS-15. It is possible that these organic molecules serve as nucleation sites for magnetite via a self-assembly mechanism. The association of proteins

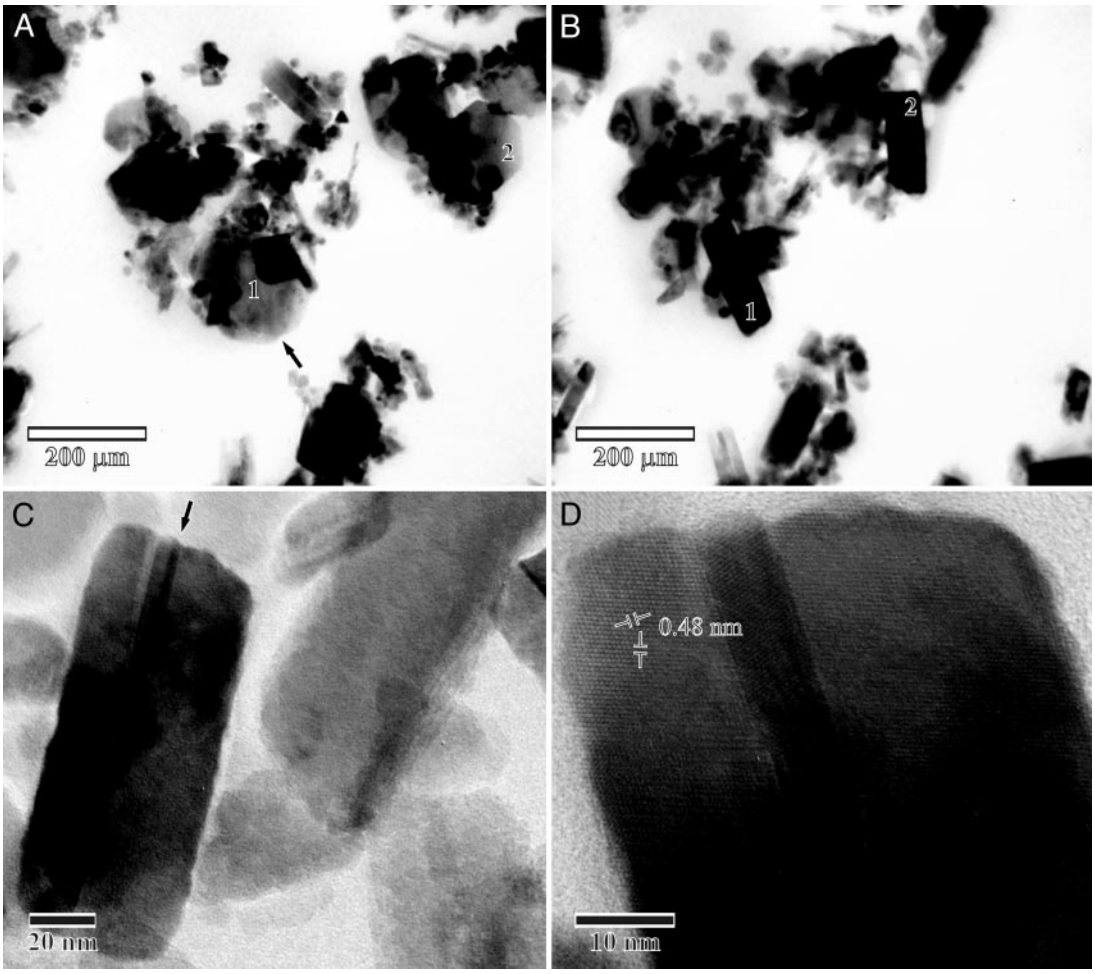

Fig. 5. TEM images obtained from ultrathin sections prepared from the sample at 668 h showing crystal shape and structure of tabular magnetite (pseudohexagonal). Projection of tabular magnetite at 0° tilting (*A*) and at 40° tilting (*B*) showing the orientation of the {111} crystal face parallel (1 and 2 in *A*) and perpendicular (1 and 2 in *B*) of the same particles with respect to the plane of the ultrathin section. (*C* and *D*) High-resolution TEM images of an individual crystal of magnetite showing two sets of {111} lattice fringes of magnetite. Arrows in *A* and *C* show twinning in magnetite crystals.

and other organic molecules has been observed in minerals such as hydroxyapatite (32), calcite (33, 34), and iron oxyhydroxide (35). It is also possible, however, that the role of bacteria is to provide a suitable environment (e.g., pH, Eh, ionic strength) for the precipitation of magnetite. If so, models proposed for inorganic mechanisms may be used to explain the formation of magnetite (36).

The tabular magnetite formed by GS-15 under the experimental conditions presented in this study is unique and has not been found, to our knowledge, in any other biological or nonbiological system. Pseudomorphic replacement, solid-state phase transformation, incorporation of impurities, the presence of a template, and epitactic growth are considered as factors responsible for the deviation from equilibrium crystal shape. There is no obvious evidence to suggest that any of the above pathways lead to the formation of the tabular-shaped magnetite in this study. Both the equilibrium shape (diamond) and tabular magnetite are present in the 558- and 668-h samples. As both types of magnetite crystals exhibit a rather broad size distribution ranging from 10 to 200 nm (suggesting a simultaneous and continuous nucleation and growth of both crystal shapes), a conversion of one form to the other can be excluded. The formation of different crystal shapes under the same experimental conditions in a closed system has been observed only in magnetotactic bacteria (5), where the nucleation and growth of magnetic crystals is controlled by a surrounding membrane (37). Banfield *et al.* (28) proposed an interesting mechanism for crystal growth in a biological system that is based on the aggregation of clusters of atoms serving as sites of nucleation for crystals. A similar mechanism may operate in our system leading to the formation of free magnetite particles. The coprecipitation of tabular and diamond shaped magnetite as free particles under the same environmental conditions cannot be explained, however, on the basis of the same kinetic and thermodynamic laws that are applied to inorganic systems. The existence of different microenvironments is required to explain this phenomenon. Indeed, we have observed within the mineral aggregates an accumulation of biomass that may create thermodynamic conditions different from the bulk environment. It is possible that a protein-based mineralization process is responsible for the formation of the magnetite in our system. Mineral formation under such a process is common in higher organisms (32, 38, 39). However, minor changes in the size and shape of the magnetite between 558 h and 34 days could result from an aging or ripening process.

Traditionally, magnetotactic bacteria and their magnetite fossils have been thought to be the predominant carriers of stable remanence in sediments (25, 40). As discussed by Lovley *et al.* (9), however, GS-15 produces 5,000-fold more magnetite than an equivalent biomass of magnetotactic bacteria, al-

though only 4% of magnetite grown under standard conditions is SD (18). Our demonstration that under some experimental conditions GS-15 produces predominantly SD magnetite suggests that GS-15 magnetite could potentially be the dominant source of magnetization in sediments. The magnitude of the actual contribution of SD GS-15 magnetite depends on how widespread the conditions under which GS-15 produces such crystals [which would include but are probably not limited to low CO_2 and unlimited Fe(III) as in our experiments] are in the environment. It is possible that although tabular minerals were observed in soils and sediments, they were not recognized as magnetite. If this magnetite is common in nature, it may be useful as a biosignature. In addition, its distinct shape and magnetic properties may be important in such fields as biomimetics and nanotechnology.

We thank John D. Coates for providing the GS-15 culture; Jeannie Mui of the McGill University Facility for Electron Microscopy Research for assistance with sample preparation for TEM; and two anonymous reviewers for their constructive comments. This work was supported by the Natural Sciences and Engineering Research Council of Canada and the Fonds Québécois de la Recherche sur la Nature et les Technologies to the Centre for Biorecognition and Biosensors (H.V.) and the American Chemical Society Petroleum Research Fund and U.S. Department of Energy Financial Assistance Award DE-FC09-96SR18546 to the University of Georgia Research Foundation (C.L.Z.).

1. Kostov, I. (1968) *Mineralogy* (Oliver and Boyd, Edinburgh).
2. Veblen, D. R. & Post, J. E. (1983) *Am. Mineral.* **68,** 790–803.
3. Bradley, J. P., McSween, H. Y. & Harvey, R. P. (1998) *Meteorit. Planet. Sci.* **33,** 765–773.
4. Vali, H., Förster, O., Amarantidis, G. & Petersen, N. (1987) *Earth Planet. Sci. Lett.* **86,** 389–400.
5. Vali, H. & Kirschvinck, J. L. (1989) *Nature* **339,** 203–206.
6. Vali, H. & Kirschvinck, J. L. (1990) in *Iron Biominerals*, eds. Frankel, R. B. & Blakemore, R. P. (Plenum, New York), pp. 97–115.
7. Zhang, C., Vali, H., Romanek, C. S., Phelps, T. J. & Liu, S. V. (1998) *Am. Mineral.* **83,** 1409–1418.
8. Roh, Y., Zhang, C. L., Vali, H., Lauf, R. J., Zhou, J. & Phelps T. J. (2003) *Clays Clay Min.* **51,** 83–95.
9. Lovley, D. R., Stolz, J. F., Nord, G. L., Jr., & Phillips, E. J. P. (1987) *Nature* **330,** 252–254.
10. Lovley, D. R. (1991) in *Iron Biominerals*, eds. Frankel, R. B. & Blakemore, R. P. (Plenum, New York), pp. 151–166.
11. Nealson, K. H. & Myers, C. R. (1990) *Am. J. Sci.* **290,** 35–45.
12. Lovley, D. R. & Phillips, E. J. P. (1988) *Appl. Environ. Microb.* **54,** 1472–1480.
13. Lovley, D. R., Giovannoni, S. J., White, D. C., Champine, J. E., Phillips, E. J. P., Gorby, Y. A. & Goodwin, S. (1993) *Arch. Microbiol.* **159,** 336–344.
14. Schwertmann, U. & Cornell, R. M. (1991) *Iron Oxides in the Laboratory* (VCH, New York).
15. Chaudhuri, S. K., Lack, J. G. & Coates, J. D. (2001) *Appl. Environ. Microbiol.* **67,** 2844–2848.
16. Zhang, C., Liu, S., Phelps, T. J., Logan, J., Mazumder, R. & Phelps, T. J. (1996) *Appl. Biochem. Biotechnol.* **57/58,** 923–932.
17. Weiss, B. P., Kim, S. S., Kirschvink, J. L., Kopp, R. E., Sankaran, M., Kobayashi, A. & Komeili, A. (2004) *Earth Planet. Sci. Lett.* **224,** 73–89.
18. Moskowitz, B., Frankel, R., Bazylinski, D., Jannash, W. & Lovley, D. (1989) *Geophys. Res. Lett.* **16,** 665–668.
19. Moskowitz, B., Frankel, R. & Bazylinski, D. A. (1993) *Earth Planet. Sci. Lett.* **120,** 283–300.
20. Muxworthy, A. R. & McClelland, E. (2000) *Geophys. J. Int.* **140,** 101–114.
21. Brabers, V. A. M., Walz, F. & Kronmuller, H. (1998) *Phys. Rev. B* **58,** 14163–14166.
22. Walz, F., Brabers, J. H. V. J. & Brabers, V. A. M. (2002) *Z. Metallkd.* **93,** 1095–1102.
23. Weiss, B. P., Kim, S. S., Kirschvink, J. L., Kopp, R. E., Sankaran, M., Kobayashi, A. & Komeili, A. (2004) *Proc. Natl. Acad. Sci. USA* **101,** 8281–8284.
24. Hirt, A. M., Lanci, L., Dobson, J., Weidler, P. & Gehring, A. U. (2002) *J. Geophys. Res. Solid Earth* **107,** B1, 2011, doi:10.1029/2001JB000242.
25. Chang, S.-B. R. & Kirschvink, J. L. (1989) *Annu. Rev. Earth Planet. Sci.* **17,** 169–195.
26. Scheffer, F. & Schachtschabel, P. (1989) *Lehrbuch der Bodenkunde* (Enke Verlag, Stuttgart), 12th Ed.
27. Lin, H., Sakamoto, H., Seo, W. S., Kuwabara, K. & Koumoto, K. (1998) *J. Crystallogr. Growth* **192,** 250–256.
28. Banfield, J. F., Welch, S. A., Zhang, H., Ebert, T. T. & Penn, R. L. (2000) *Science* **289,** 751–754.
29. Lowenstam, H. A. & Weiner, S. (1989) *On Biomineralization* (Oxford Univ. Press, New York).
30. Mann, S., Sparks, N. H. C. & Wade, V. J. (1990) in *Iron Biominerals*, eds. Frankel, R. B. & Blakemore, R. P. (Plenum, New York), pp. 21–49.
31. Newman, D. K. & Banfield, J. F. (2002) *Science* **296,** 1071–1077.
32. Vali, H., McKee, M. D., Ciftcioglu, N., Sears, S. K., Plows, F. L., Chevet, E., Plavsic, M., Kajander, E. O. & Zare, R. N. (2001) *Geochem. Cosmochem. Acta* **65,** 63–74.
33. Addadi, L. & Weiner, S. (2001) *Nature* **411,** 753–754.
34. Beniash, E., Traub, W., Veis, A. & Weiner, S. (2001) *J. Struct. Biol.* **135,** 8–17.
35. Chan, C. S., De Stasio, G., Welch, S. A., Girasole, M., Frazer, B. H., Nesterova, M. V., Fakra, S. & Banfield, J. (2004) *Science* **303,** 1656–1658.
36. Tamaura, Y., Saturno, M., Yamada, K. & Katsura, T. (1984) *Bull. Chem. Soc. Jpn.* **57,** 2417–2421.
37. Komeili, A., Vali, H., Beveridge, T. J. & Newman, D. K. (2004) *Proc. Natl. Acad. Sci. USA* **101,** 3839–3844.
38. Mann, S. & Weiner, S. (1999) *J. Struct. Biol.* **126,** 179–181.
39. Mann, S. Sparks, N. H. C. & Board, R. G. (1991) *Adv. Microb. Physiol.* **31,** 125–181.
40. Petersen, N., von Dobeneck, T. & Vali, H. (1986) *Nature* **320,** 611–615.